PCCP

ROYAL SOCIETY OF CHEMISTRY

PAPER

View Article Online
View Journal | View Issue

Cite this: *Phys. Chem. Chem. Phys.*, 2025, **27**, 19772

A DFT study on the curving of 4N-divacancy defected graphene quantum dots induced by an external electric field and the effects of metal-ion doping

Thanawit Kuamit, Wilasinee Santiwarodom, Pavee Apilardmongkol, Sirilak Kongkaew and Vudhichai Parasuk *

We conducted a study to examine the impact of an external electric field on the curvature of metal and divalent metal ion doped 4N divacancy-defected graphene quantum dots (4N-GQDs), utilizing Density Functional Theory (DFT). We considered six common metal species, namely Ca, Ca^{2+}, Cr, Cr^{2+}, Fe, and Fe^{2+}. Our findings reveal that the curvature of metal and divalent metal ion-doped-4N-GQDs increases as the external electric field strength rises in both positive and negative directions. However, the direction of curvature is contingent upon the orientation of the electric field, which is perpendicular to the 4N-GQD plane. The curvature directions of metal and divalent metal ion-doped-4N-GQDs under positive and negative electric fields are opposite. It is interesting to note that the HOMO–LUMO gap of metal and divalent metal ion doped 4N-GQDs can be altered by applying an external electric field exceeding ±0.020 a.u. Within this context, the gap for 4N-GQDs doped with these ions typically spans from 1.64 to 2.98 eV, which is lower than that of GQDs and undoped 4N-GQDs. As a result, we advocate a technique to deliberately induce curvature for metal and divalent metal ion-doped 4N-GQDs, thereby altering their electronic properties through the application of an external electric field. These materials show substantial promise as anchoring materials for electronic devices.

Received 7th June 2025,
Accepted 9th August 2025

DOI: 10.1039/d5cp02152a

rsc.li/pccp

Introduction

Graphene is a one-atom-thick, two-dimensional carbon allotrope with sp^2-hybridized atoms, derived from graphite.[1] Its outstanding electrical conductivity, thermal stability, high surface area, and light weight make it suitable for applications in drug delivery,[2,3] semiconductors,[4–7] energy storage,[8–10] biosensors,[11] solar cells,[12–14] and gas adsorption.[15–18] A key research focus is modifying graphene into a semiconductor, especially through deformation or curvature to tune its electronic properties.[19–23] Recent studies have shown that curvature significantly impacts the electronic properties of graphene quantum dots (GQDs), offering promising insights for nanoelectronics.[24] Chang *et al.*[25] found that exceeding a threshold arc angle θ in curved armchair graphene nanoribbons markedly alters their electronic structure. Pattarapongdilok *et al.*[26] reported that increased folding of GQDs reduces the HOMO–LUMO gap, highlighting their potential for electronic and optical devices. Several techniques have been developed to induce curvature in graphene: Bao *et al.*[27] used thermomechanical methods to generate periodic ripples, Georgiou *et al.*[28] controlled graphene bubbles *via* electric fields, Zhang *et al.*[29] investigated nanoribbon bending through molecular chemisorption, and other studies[30] showed that liquid droplets can significantly deform graphene surfaces.

Recent studies have focused on vacancy defects in graphene, analyzing their effects on mechanical, electrical, and thermal properties. Researchers have investigated various defects, including Stone–Wales defects,[31,32] single vacancy defects,[33] multiple vacancy defects,[34] and substitutional impurities.[35–37] Nitrogen doping has emerged as an effective method for tailoring graphene's properties, expanding its applications in gas adsorption,[38] batteries,[39] hydrogen storage materials,[40,41] and particularly in nanoelectronics.[42] 4N-divacancy defected graphene quantum dots (4N-GQDs), when doped with transition metals, offer a promising approach for band gap engineering, a critical aspect for their integration into nanoelectronic devices.[43,44] Incorporating metal atoms into the cavities of 4N-GQDs introduces localized electronic states and modifies the overall electronic structure, enabling tunable semiconducting properties essential for transistor-based applications. For instance, a study by Jiménez-Ramírez *et al.*[45] employed first-principles calculations to investigate transition metal adsorption on porphyrin-like motifs in pyrrolic nitrogen-

Center of Excellence in Computational Chemistry (CECC), Department of Chemistry, Faculty of Science, Chulalongkorn University, Pathumwan, Bangkok 10330, Thailand. E-mail: Vudhichai.P@chula.ac.th

doped carbon nanostructures. The research demonstrated that such configurations could effectively tailor the electronic properties of graphene, making them suitable for nanoelectronic applications. Among various synthesis techniques, chemical vapor deposition has proven most effective for nitrogen doping, producing distinct defect structures such as graphitic (where nitrogen replaces a carbon atom), pyridinic (where three nitrogen atoms surround a vacancy), and porphyrin-like (where four nitrogen atoms form a divacancy) configurations.[46,47]

Graphene quantum dots (GQDs), consisting of single- or few-layer graphene with lateral dimensions smaller than 100 nm, have gained attention for their potential applications in numerous fields.[48–52] GQD fabrication follows two main approaches: top-down and bottom-up. The top-down approach involves extracting GQDs from larger graphene sheets using techniques such as electrochemical exfoliation, ultrasonication, acidic oxidation, electron beam lithography, and chemical exfoliation. In contrast, the bottom-up approach synthesizes GQDs from polycyclic aromatic compounds or aromatic-structured molecules using processes like pyrolysis, carbonization, fullerene cage-opening, microwave synthesis, hydrothermal and solvothermal methods, and templating techniques.[53,54]

Extensive research has also explored the influence of electric fields on GQDs. Shen[55] used B3LYP/6-31G* calculations to demonstrate that an external electric field can induce deformation, modify polarization-charge distribution, and influence the dipole moment of graphene. Wang[56] employed a simplified model to predict the field-induced alignment of cantilevered graphene nanoribbons (GNRs), showing that their equilibrium structures depend on electric field strength, with a linear relationship between the alignment angle and the square of field strength. Haipeng *et al.*[57] examined how external electric fields affect the electronic structure and hyperpolarizability of hexagonal GQDs, showing that strong electric fields along the *z*-axis cause GQDs to bend, significantly reducing their frontier orbital energy gap. In our prior study,[58] we analyzed the curvature of three different GQD sizes ($C_{24}H_{12}$, $C_{54}H_{18}$, and $C_{96}H_{24}$) under vertical external electric fields using density functional theory (DFT). Our findings indicated that the curvature of GQDs depends on the field strength and that their HOMO–LUMO gap decreases as the field strength increases. These results confirm that an external electric field can induce curvature in GQDs, providing a means to modulate their electronic properties. Based on the literature, external electric fields can modulate the HOMO–LUMO gap of graphene and induce structural deformations, such as curvature, which can be harnessed for nanoelectronic applications. Since experimental measurements of these nanoscale effects remain challenging, computational studies have become a primary tool for investigating electric field effects on nanomaterials. Our previous research[58] examined the impact of electric fields on symmetric GQDs. In addition, Bhattacharyya *et al.*[59] also conducted a study on the effect of an external electric field on coronene, suggesting that the structure undergoes non-spontaneous structural distortion, such as curving or puckering, when exposed to a sufficiently strong external electric field. This deformation is primarily driven by intramolecular charge redistribution rather than vibronic interactions like the pseudo Jahn–Teller effect. However, the behaviour of unsymmetrical 4N-divacancy-defected GQDs (4N-GQDs), which have a porphyrin-like structure and can incorporate metal/metal ions, remains unexplored.

In this study, we employed DFT calculations to investigate the molecular structures and electronic characteristics of 4N-GQDs and metal/metal-ion-doped 4N-GQDs (M–4N-GQDs, where M = Ca, Ca^{2+}, Cr, Cr^{2+}, Fe, and Fe^{2+}) under vertical electric fields. Due to the challenges of experimental studies on graphene-like structures, DFT calculations provide a suitable approach. We propose an innovative method to control the curvature of 4N-GQDs/M–4N-GQDs using external electric fields, potentially enabling new applications in nanoelectronic devices.

Computational methods

All calculations were conducted using density functional theory (DFT) within the Gaussian16 software,[60] employing the 6-31G(d) basis set. The exchange–correlation interactions were described using the meta-generalized gradient approximation (meta-GGA) with the M06-2X functional. The M06-2X functional is well-suited for studying graphene due to its balanced handling of exchange–correlation interactions and its reliable accuracy in modeling electron delocalization.[61,62] The self-consistent field (SCF) calculations were performed with a convergence threshold of 10^{-6} atomic units.

To model graphene quantum dots (GQDs), $C_{96}H_{24}$ also known as circumcircumcoronene was selected due to its hexagonal symmetry, structural stability, and status as the largest fully hydrogenated species in its class.[63,64] The 4N-divacancy-defected GQD (4N-GQD) structure was generated by removing two carbon atoms and subsequently substituting four surrounding carbon atoms with nitrogen. To further investigate the effects of metal doping, six metal-embedded 4N-GQDs (M–4N-GQDs) were created by incorporating Ca, Ca^{2+}, Cr, Cr^{2+}, Fe, and Fe^{2+} into the nitrogen-doped vacancy.

The influence of an external electric field (EF) on the molecular and electronic properties of both 4N-GQDs and M–4N-GQDs was analyzed by applying a perpendicular field with strengths ranging from −0.030 to +0.030 atomic units. Schematic representations of GQDs, 4N-GQDs, and M–4N-GQDs, along with the applied field direction, are illustrated in Fig. 1.

Results and discussion

Impact of an external electric field on metal binding

The complexation energy ($E_{complex}$) is evaluated to assert the metal binding to 4N-GQDs and their values are displayed in Fig. 2 and Table S1 of the SI.

$$E_{complex} = E_{M-4N\text{-}GQDs} - E_{4N\text{-}GQDs} - E_{M} \quad (1)$$

In the absence of an external electric field, the binding was found between 5.4 and 20.4 eV. The binding of Fe is the weakest, and those of Cr^{2+} and Ca^{2+} are the strongest. In general, the

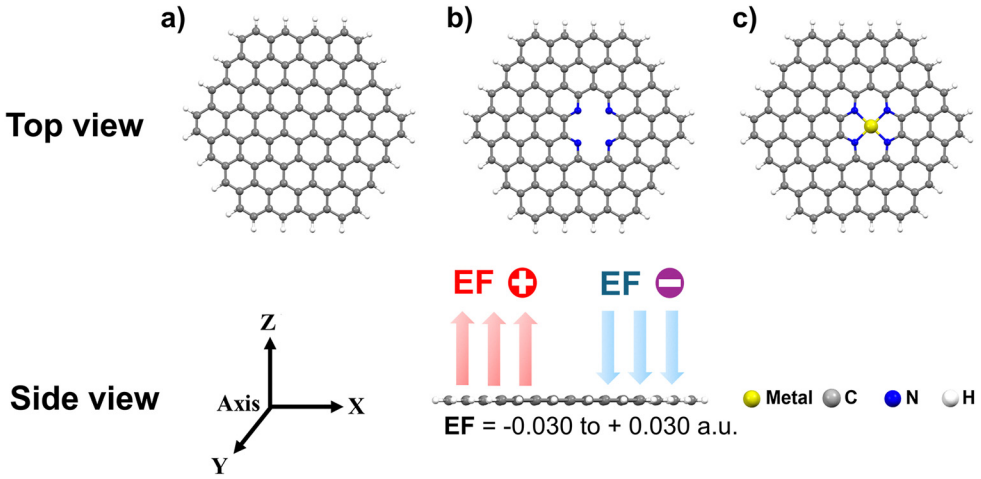

Fig. 1 The geometry of (a) GQDs, (b) 4N-GQDs, and (c) M–4N-GQDs, along with the direction of the applied field.

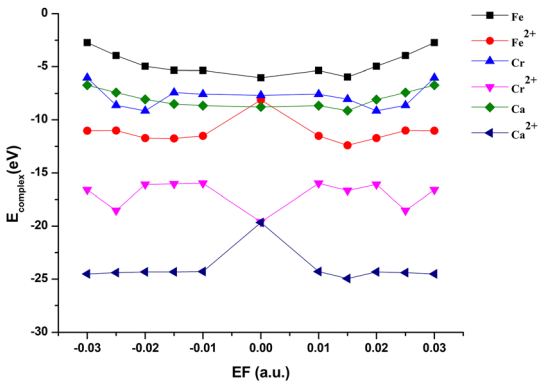

Fig. 2 The complexation energy ($E_{complex}$) of metal and metal(II)–4N-GQDs with different electric fields.

binding of 4N-GQDs with bare metals is weaker than with metal ions, realizing that 4N-GQDs are neutral compounds. Under the influence of an electric field, the binding of bare metal (Ca, Fe, and Cr) does not significantly vary, while a more pronounced change was observed for the binding of metal ions (Ca^{2+}, Fe^{2+}, and Cr^{2+}). However, the field direction does not affect the binding of metal/metal ions to 4N-GQDs. For Ca^{2+} and Cr^{2+}, the binding was found to increase with the field, while it decreased for Fe^{2+}. Thus, the metal binding can be enhanced/unenhanced by an electric field.

Impact of an external electric field on the molecular geometry

After applying an external electric field (EF), all structures (4N-GQDs and M–4N-GQDs) were found to be curved. This curving of the structure is spotted from the rise of *z*-coordinates (from before applying fields, which are generally zeroes). Thus, the variation in the *z*-coordinate (ΔZ) was determined to assess the structure's curving. Two distinct directions of curvature were observed, *i.e.*, along the C atom and C–C bond directions, as illustrated in Fig. 3. The curving of the structure is similar to what was observed in our previous finding of graphene quantum dots (GQDs).[58] The optimized geometries of metal and divalent metal ion-doped 4N-GQDs are displayed in Fig. 4 and 5, respectively. For 4N-GQDs, the optimized geometry under various vertical electric fields is shown in Fig. S1, SI.

As the strength of the field increases, the curvature of the metal- and metal ion-doped 4N-GQDs also increases. This curvature aligns with the orientation of the electric field along the *Z*-axis, which is perpendicular to the plane of the GQDs. Under a positive field direction, both bare metals and divalent metal ion doped 4N-GQDs display a convex curvature, while they exhibit a concave curvature in a negative field direction. For most M–4N-GQDs, the metal/metal ion is placed in the center of the 4N cavity of 4N-GQDs, even under an external electric field, except for Ca/Ca^{2+}. For Ca/Ca^{2+}, we observed the displacement of the metal from the center of the complex. The displacement of Ca and Ca^{2+} is due to their larger size as compared to other metals. Consequently, the field strength influences the degree of curvature of M–4N-GQDs. From Fig. 6 and 7, the observation indicates that metal- and metal ion-doped 4N-GQDs bend more explicitly along

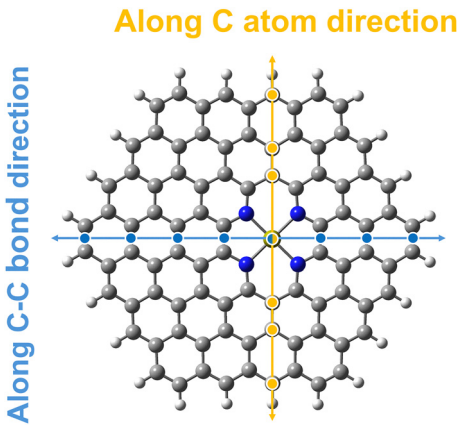

Fig. 3 Two curving directions of metal and metal(II)–4N-GQDs: along C atom and C–C bond directions.

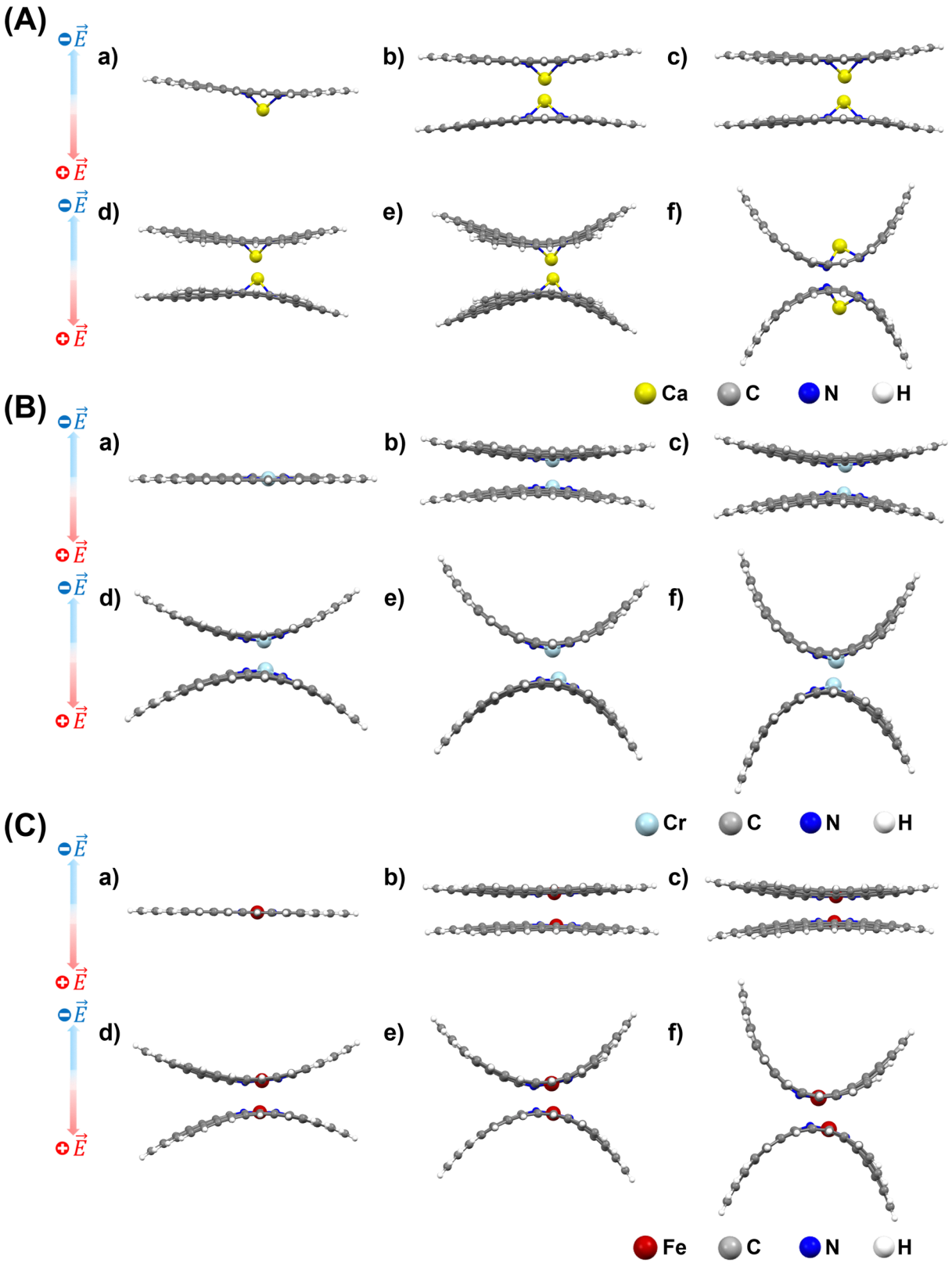

Fig. 4 Geometry optimization of the M–4N-GQDs model for (A) Ca, (B) Cr, and (C) Fe under varying electric fields: (a) 0.0 a.u., (b) 0.010 a.u., (c) 0.0150 a.u., (d) 0.020 a.u., (e) 0.025 a.u., and (f) 0.030 a.u.

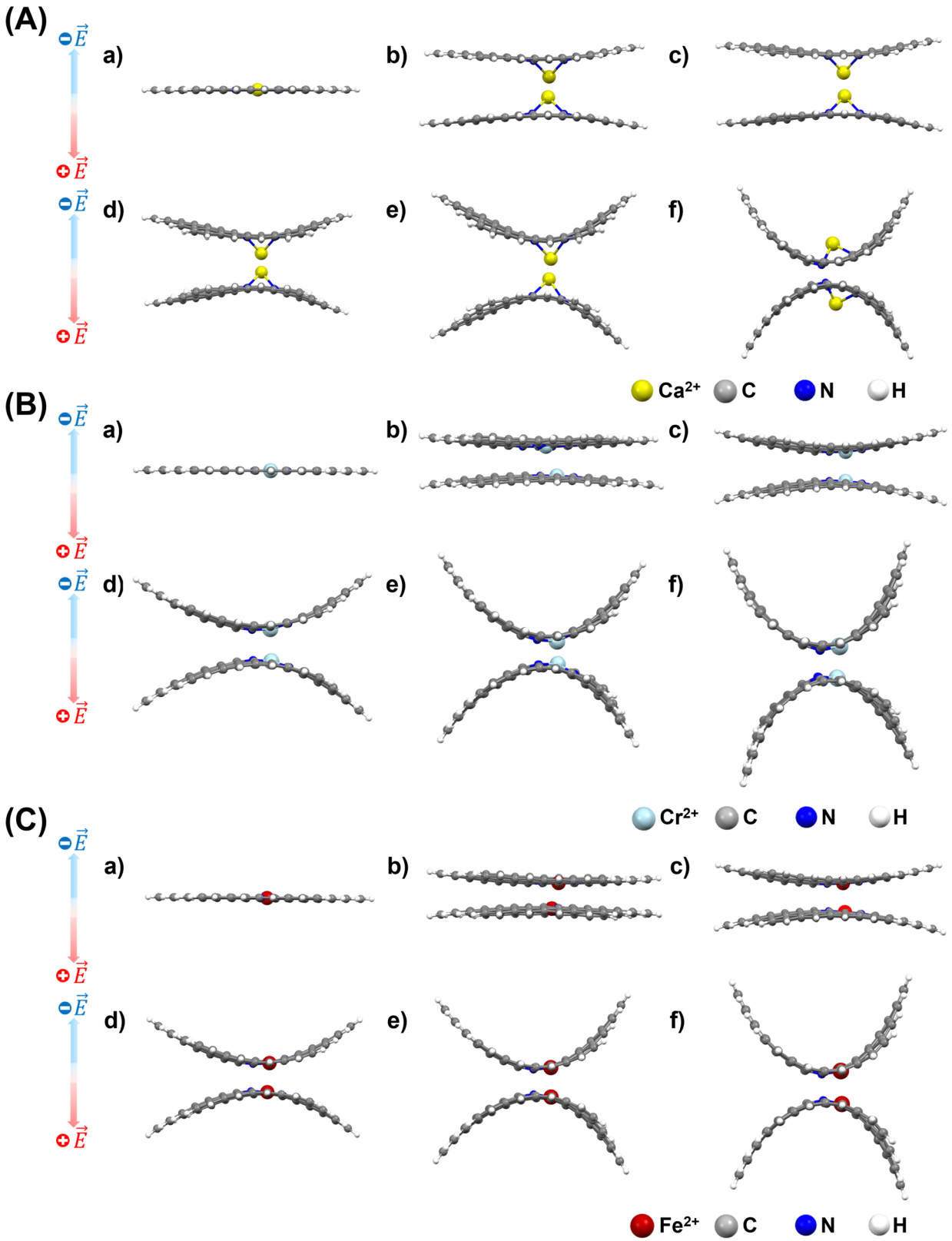

Fig. 5 Geometry optimization of the M^{2+}–4N-GQD model for (A) Ca^{2+}, (B) Cr^{2+}, and (C) Fe^{2+} under varying electric fields: (a) 0.0 a.u., (b) 0.010 a.u., (c) 0.0150 a.u., (d) 0.020 a.u., (e) 0.025 a.u., and (f) 0.030 a.u.

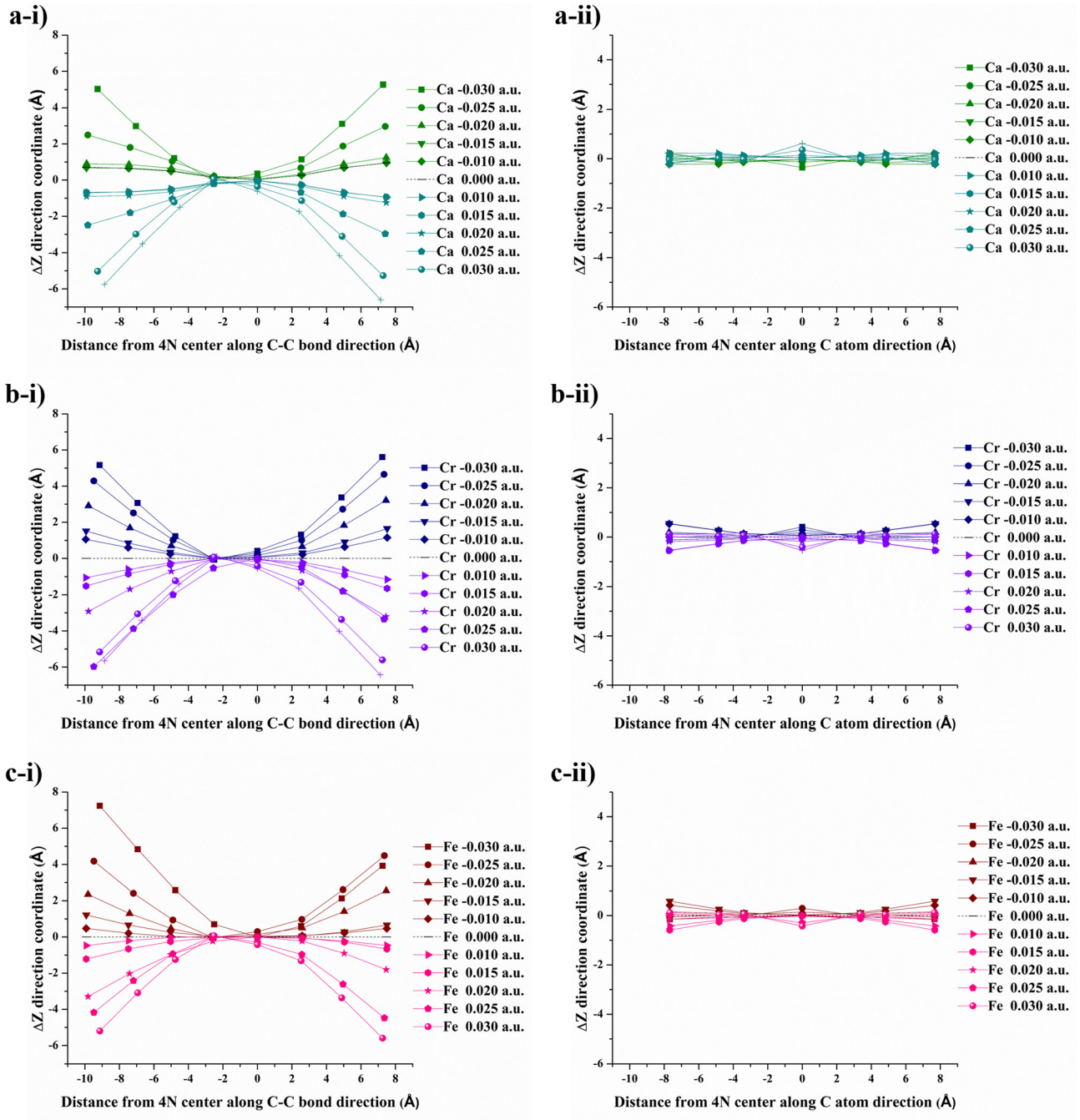

Fig. 6 Plots of variations in Z coordinates (ΔZ) and the distance from the 4N center (in Å) for: (a) Ca–4N-GQDs, (b) Cr–4N-GQDs, and (c) Fe–4N-GQDs, where (i) represents the direction along the C–C bond, and (ii) represents the direction along the C atom, under an external electric field ranging from −0.030 to +0.030 a.u.

the C–C bond direction than along the C atom direction. The curving of 4N-GQDs tends to occur along the C–C bond direction, as illustrated in Fig. S2. Similar to our previous publication,[58] we found that, for a particular field strength, the plot of ΔZ and the distance from the 4N center can be quantified by a quadratic equation, $y = ax^2 + bx + c$, with R^2 of the fit exceeding 0.97.

Exceptions are those for Ca and Ca^{2+} doped 4N-GQDs where R^2 fitting is less than 0.97 but still greater than 0.90. The exclusion of the results of Ca/Ca^{2+} doped 4N-GQDs might come from the fact that for these complexes, Ca/Ca^{2+} does not occupy the center of the 4N cavity. The quadratic equations, together with their R^2 for GQDs, 4N-GQDs, and M–4N-GQDs, are presented in Tables S2–S4, SI. We could match the coefficient 'a' with the largest bending angle θ, which is defined as the angle of the slope of the line connecting the 4N center with GQDs' edge, as portrayed in Fig. 8. For unsymmetrical GQDs, there are 2 angles, the angle to the left (θ_1) and right (θ_2) of the 4N center. The relation between θ and the coefficient 'a' can

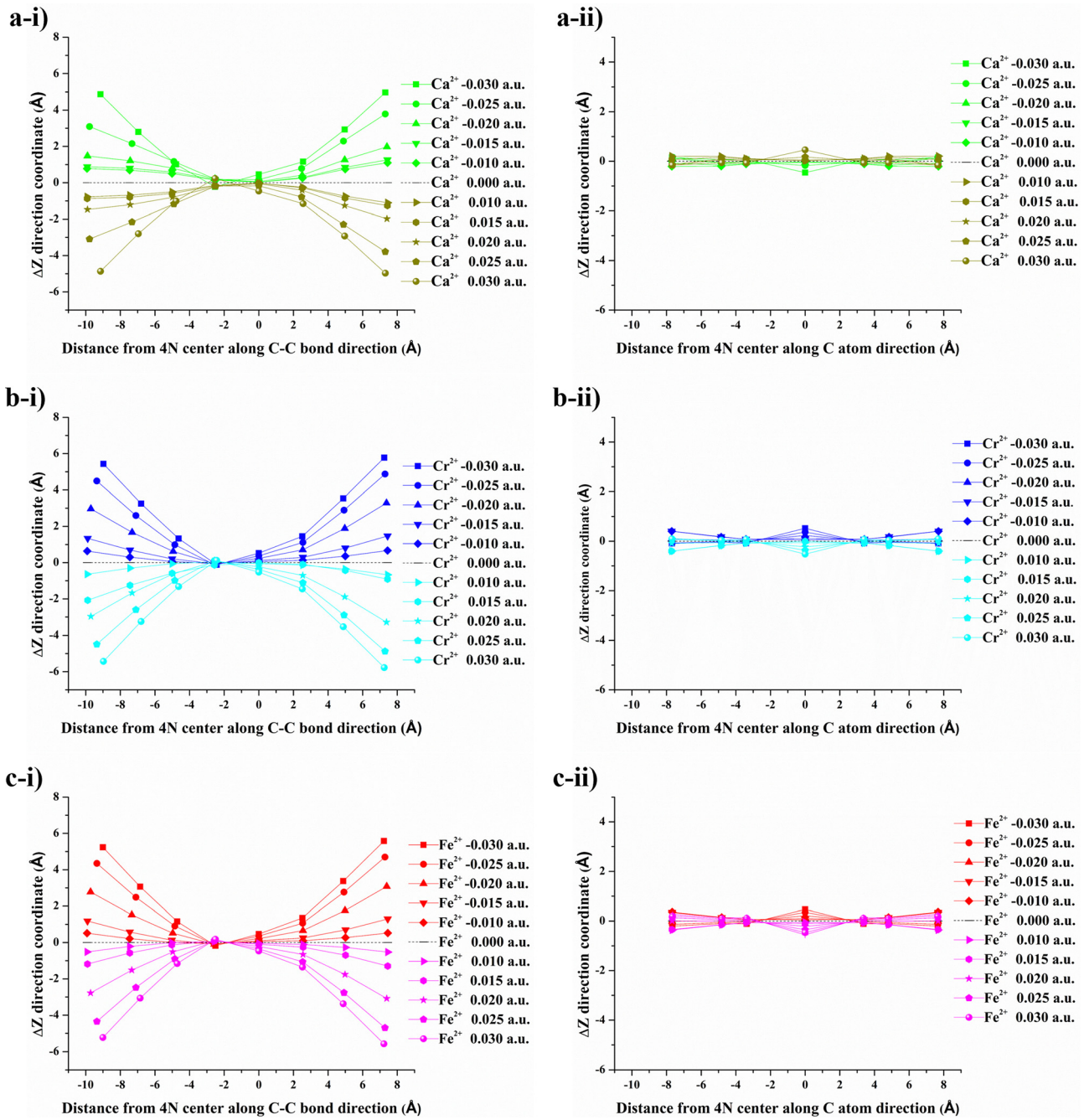

Fig. 7 Plots of variations in Z coordinates (ΔZ) and distance from the 4N center (in Å) for: (a) Ca^{2+}–4N-GQDs, (b) Cr^{2+}–4N-GQDs, and (c) Fe^{2+}–4N-GQDs, where (i) represents the direction along the C–C bond, and (ii) represents the direction along the C atom, under an external electric field ranging from −0.030 to +0.030 a.u.

be ratified by the following equations.

$$\theta_1 = \tan^{-1}\left(\frac{y_1 - e}{x_1 - d}\right)$$

$$\theta_2 = \tan^{-1}\left(\frac{y_2 - e}{x_2 + d}\right)$$

Where $d = \frac{b}{2a}$ and $e = c - \frac{b^2}{4a}$.

The dependency of θ_1 and θ_2 with field strength for GQDs, 4N-GQDs, and M–4N-GQDs is shown in Tables S5–S8 in the SI. For the strongest field (EF = ±0.030 a.u.), the largest bending angle ranges between 270 and 360, in which GQDs have the smallest bending angle. This suggests GQDs to be stiffer, and the defect causes the structures to be more flexible. Unlike other structures, GQDs have the same value for θ_1 and θ_2 at the same EF owing to their symmetric geometry. The bending angle of 4N-GQDs is slightly smaller than that of M–4N-GQDs, and θ_1

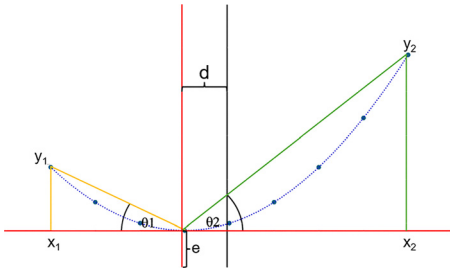

Fig. 8 The coefficient *a* with the largest bending angle θ, which is defined as the angle of the slope of the line connecting the 4N center with the GQDs' edge.

is smaller than θ_2, while for other structures $\theta_1 > \theta_2$. Thus, embedding metal makes the structure more flexible. Among M–4N-GQDs, the largest bending angle does not differ much, implying that the bending of graphene quantum dots is not associated with the types of metals. Interestingly, the relationship between θ_1 and θ_2 with the coefficient '*a*' is linear, as shown in Fig. S3–S8, SI. Thus, $|a|$ (absolute value of '*a*') can be used to describe the degree of curvature for these graphene quantum dots.

As the electric field strength increases for both directions, the degrees of curvature $|a|$ for GQDs, 4N-GQDs, and metal/metal ion-doped 4N-GQDs demonstrate a consistent rise. Fig. 9 provides the relation of the electric field strength and the degrees of curvature $|a|$ for GQDs, 4N-GQDs, and metal/metal ion-doped 4N-GQDs. From the plot, the degree of curvature for M–4N-GQDs shows symmetric dependence on the electric field with similar values for $|a|$, except for Ca–4N-GQDs. At EF = 0, the $|a|$ value of Ca–4N-GQDs is non-zero, which means that the structure is not planar (its $\theta_1 = 7.010$) even at zero field. For this complex, the structure starts to curve further after EF above $\pm$0.020 a.u. (The $|a|$ remains the same for EF = 0.000, $\pm$0.010, and $\pm$0.020 a.u.) From Fig. 9, 4N-GQDs display higher $|a|$, while their $|a|$ values are lower for GQDs. This feature is similar to our discussion on θ, which suggests that $|a|$ and θ are dependent.

Pattarapongdilok and Parasuk[26] reported very large deformation energy for GQDs. We are interested in knowing what

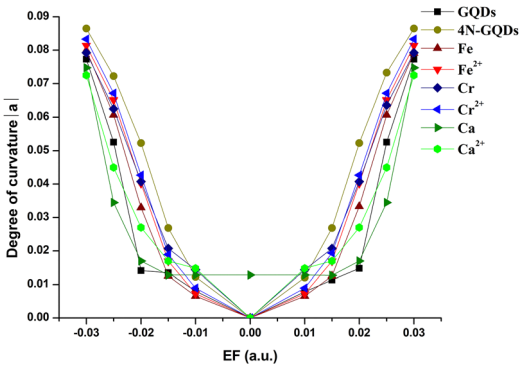

Fig. 9 The degrees of curvature for GQDs, 4N-GQDs, metal- and metal ion-doped 4N-GQDs at various electric fields.

facilitates the curving of graphene quantum dots. The dipole moment of the GQD-related structure increases significantly as the structure changes from flat to curved. Under an external electric field, molecules with a permanent dipole moment can be stabilized, as shown in Tables S9 and S10. By neglecting higher-order terms, the energy of molecules under the influence of an external electric field ($E(F)$) can be expressed by

$$E(F) = E_0 - \mu F \quad (2)$$

where μ is the permanent dipole moment and F is the field.

Indeed, for GQDs, 4N-GQDs, and M–4N-GQDs their dipole moments are large and become larger at a stronger field. Values of $-\mu F$ of M–4N-GQDs, M = Ca, Cr, Fe, Ca^{2+}, Cr^{2+}, and Fe^{2+}, under external electric fields ranging from -0.030 to $+0.030$ atomic units are given in Tables 1 and 2. To rationalize the above hypothesis, deformation energies (E_{def}) and dipole interaction ($-\mu F$) for six M–4N-GQDs were estimated and are reported in Tables 1 and 2. E_{def} is determined according to

$$E_{def} = E_{0,EF} - E_{0,noEF} \quad (3)$$

$E_{0,EF}$ is the energy of M–4N-GQD at EF when turning off the field (or E_0 from eqn (2)), and $E_{0,noEF}$ is the energy of M–4N-GQD at EF = 0.

From Tables 1 and 2, the field dependent of the deformation energies of M–4N-GQDs was observed and can be visualized in Fig. 10. The deformation energy of M–4N-GQDs at the same field strength but different directions ($\pm$) has the same value. Fig. 10 has a similar profile to Fig. 9, the plot between the degree of curvature and field strength. Thus, the deformation of energy can be related to the degree of curvature and the curving of M–4N-GQDs. The plot of E_{def} with the field strength of Fe–4N-GQDs lies above the others. This suggests that Fe doping causes the bending of M–4N-GQDs to be least favorable. Most M–4N-GQDs have positive and large deformation energies, which suggests that the curving of M–4N-GQDs is unfavorable (the structure is very stiff). However, Ca^{2+}–4N-GQDs under an EF between -0.020 and $+0.020$ a.u. has negative deformation energies. We also observed the association between the degree of curvature and permanent dipole moment. The linear regression between $|a|$ and μ at various field strengths has $R^2 > 0.95$

Table 1 Deformation energy (E_{def}) and dipole interaction ($-\mu F$) in eV of Ca/Cr/Fe–4N-GDQs under field strength from -0.030 to $+0.030$ a.u

	Ca		Cr		Fe	
EF (a.u.)	E_{def}	$-\mu F$	E_{def}	$-\mu F$	E_{def}	$-\mu F$
0.03	13.05	−18.77	13.56	−20.06	42.53	−19.08
0.025	5.09	−8.48	4.60	−10.38	22.49	−10.18
0.02	2.96	−4.92	1.13	−4.90	9.36	−4.41
0.015	2.06	−2.92	0.83	−2.17	4.25	−2.07
0.01	1.50	−1.50	0.49	−0.94	1.81	−0.88
0	0.00	0.00	0.00	0.00	0.00	0.00
−0.01	1.50	−1.50	0.49	−0.94	1.81	−0.88
−0.015	2.06	−2.92	0.83	−2.17	4.25	−2.07
−0.02	2.96	−4.92	1.13	−4.90	9.36	−4.41
−0.025	5.09	−8.48	4.60	−10.38	22.49	−10.18
−0.03	13.05	−18.77	13.56	−20.06	42.53	−19.08

Table 2 Deformation energy (E_{def}) and dipole interaction ($-\mu F$) in eV of Ca^{2+}/Cr^{2+}/Fe^{2+}–4N-GDQs under field strength from −0.030 to +0.030 a.u

	Ca^{2+}		Cr^{2+}		Fe^{2+}	
EF (a.u.)	E_{def}	$-\mu F$	E_{def}	$-\mu F$	E_{def}	$-\mu F$
0.03	9.74	−19.97	14.98	−22.95	13.98	−21.56
0.025	2.21	−9.36	5.80	−12.63	7.80	−12.19
0.02	−0.71	−5.12	3.34	−5.73	3.15	−5.45
0.015	−1.78	−2.97	1.15	−2.34	1.11	−2.26
0.01	−2.36	−1.51	0.45	−0.96	0.44	−0.93
0	0.00	0.00	0.00	0.00	0.00	0.00
−0.01	−2.36	−1.51	0.45	−0.96	0.44	−0.93
−0.015	−1.78	−2.97	1.15	−2.34	1.11	−2.26
−0.02	−0.71	−5.12	3.34	−5.73	3.15	−5.45
−0.025	2.21	−9.36	5.80	−12.63	7.80	−12.19
−0.03	9.74	−19.97	14.98	−22.95	13.98	−21.56

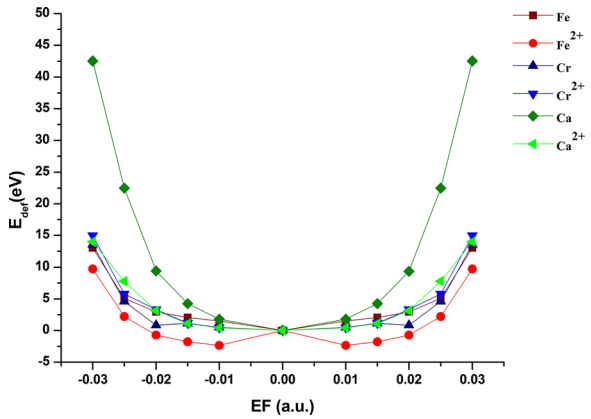

Fig. 10 The deformation energy (E_{def}) metal- and metal ion-doped 4N-GQDs at various electric fields.

for all M–4N-GQDs. Thus, the strong curving causes the structure to exhibit a large dipole moment. Although E_{def} is quite high, we found $-\mu F$ to be larger than E_{def} for most structures. This facilitates the curving of M–4N-GQDs and supports our hypothesis. Thus, the curving of M–4N-GQDs under the external electric field is driven by the large dipole moment of the structure. We monitored the effect of the electric field on nuclear repulsion energy as well as electronic energy, Fig. S9 and S11, SI. The nuclear repulsion energy increases with the increase of EEF, while the electronic energy declines. Thus, the structure is stabilized by the electron interaction and destabilized by the interaction between nuclei. The observation supports the hypothesis given by Bhattacharyya *et al.*[59]

According to eqn (2) and (3), $E(F) - E(0) = E_{def} - \mu F$. This is true for all M–4N-GQDs, except Fe–4N-GQDs. This implies that eqn (2) cannot be applied to Fe–4N-GQD. The higher multipole moment terms are important for this system, in which they cannot be neglected. Thus, the deformation energy estimated for Fe–4N-GQDs is too high. With corrections to higher multipole moment terms, the deformation energy would become lower and might be on par with other systems. At a certain EF, Ca^{2+}–4N-GQDs have a negative E_{def}. The curving of Ca^{2+}–4N-GQDs can happen even without applying an electric field (up to θ_1 = 14.570 and θ_2 = 8.840). We tested for $E(F) - E(0) = E_{def} - \mu F$, and the relation holds. This hints that the determination of E_{def} is reliable for this case. Therefore, by doping with Ca^{2+}, 4N-GQDs could be curved.

Effect of an external field on the electronic structure

The HOMO–LUMO gap (E_g) of GQDs, 4N-GQDs, metal- and metal ion-doped 4N-GDQs under varying external electric fields is depicted in Fig. 11. The HOMO and LUMO energy gaps (E_g) of GQDs, 4N-GQDs, metal-doped 4N-GQDs, and metal-ion-doped 4N-GQDs show field-dependent behavior. The trend of the HOMO–LUMO gap follows the order: GQDs (3.4 eV) > 4N-GQDs (3.0 eV) > metal–4N-GQDs (2.8 eV) > Ca–4N-GQDs (2.5 eV) > Ca^{2+}–4N-GQDs (2.3 eV) > metal ion–4N-GQDs (2.0). The HOMO–LUMO gap alters with doping species (bare metal or metal ion) rather than the types of elements.

Additionally, the field dependency of HOMO and LUMO energies of these materials is displayed in Fig. S11, SI, compared to those of pristine GQDs, while their LUMOs are lower. The HOMOs of metal doped 4N-GQDs are higher than those of undoped 4N-GQDs and pristine graphene, while their LUMOs show a similar field pattern to 4N-GQDs. The doping with metal ions shifts their HOMO and LUMO levels lower by 5 eV. Both HOMO and LUMO energies increase with the increment of an external electric field. Interestingly, Ca and Ca^{2+} doped 4N-GQDs reveal the trend discontinuity at a certain field strength, like in the case of charge transfer. The pristine GQDs have the largest band gap energy of 3.8 eV at EEF = 0.00 a.u. The band gap energy reduces drastically to around 3 eV for 4N-GQDs and metal-doped 4N-GQDs. With metal-ion doping, the band gap further reduces to around 2 eV. Thus, the electric field has a significant influence on the electron distribution and frontier orbital energies, which aligns with the conclusion made by Bhattacharyya *et al.*[59]

For most graphene quantum dots, E_g is unvaried between EF = −0.015 and +0.015 a.u. If the field strength further increases beyond those values, we found a sudden drop in

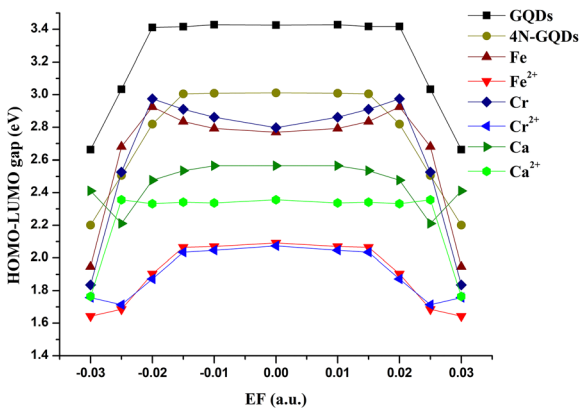

Fig. 11 HOMO–LUMO gap energies of GQDs, 4N-GQDs, metal and metal(II) ions within 4N-GDQs at different electric fields.

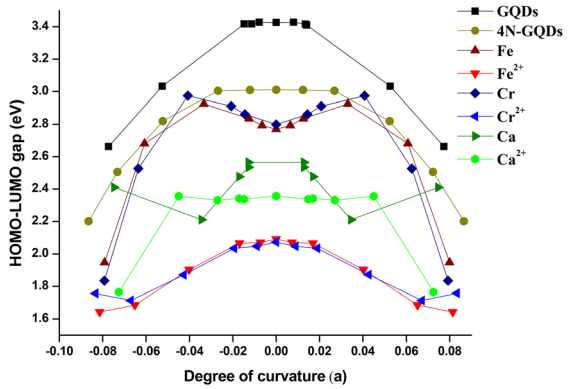

Fig. 12 The degree of curvature (|*a*|) and the evaluation of HOMO–LUMO gap energies for metal and metal(II) ion 4N-GQDs.

values of E_g, down to 1.6 eV for Fe^{2+}–4N-GQDs. For Ca– and Cr^{2+}–4N-GQDs, E_g increases again after EF = 0.025 a.u.

Fig. 12 shows the plot between the coefficient '*a*' and E_g. The trend for E_g with curvature in Fig. 12 seems to be in line with the plot in Fig. 11. The HOMO–LUMO gap for all structures is found to be unchanging during a range of *a*, then after certain values, the sudden drop of E_g is noticed. From this, we can deduce that the curving of graphene quantum dots causes values of E_g to change. But this can be observed only at large degrees of bending.

We observed the Mulliken charge and charge transfer from the metal and metal ions to the 4N-GQDs, as shown in Table S9 and Fig. S12, SI, respectively. However, the direction of electron transfer depends on the doping. For metal-atom (Ca, Cr, and Fe) doping, we found electrons being transferred from the metal atom to the 4N-GQD ligand. For metal-ion (Ca^{2+}, Cr^{2+}, and Fe^{2+}) doping, the opposite direction (from the ligand to the metal ion) was observed. The degree of transfer is related to the types of metal and the strength of the field. This figure shows charge transfer, where a negative charge indicates electron transfer from the ligand. In the case of the metal atoms Cr and Fe, the behavior is the same: transfer from the metal increases as the electric field becomes stronger. However, for Ca, the transfer decreases as the field increases, but increases again at ± 0.03. For the metal ions, the behavior differs in all three cases. For Cr^{2+}, the transfer from the ligand to the metal decreases, while for Fe^{2+}, it increases. Ca^{2+} exhibits behavior similar to that of Ca. This explains why Ca and Ca^{2+}-doped 4N-GQDs shift from the outer curvature to the inner curvature at an electric field strength of 0.03 a.u., depending on the charge transfer.

Conclusion

The binding of metal (Ca, Cr, Fe)/metal ion (Ca^{2+}, Cr^{2+}, Fe^{2+}) to 4N-GQDs varies with the types of metals and metal ions. Metal ions bind to 4N-GQDs more strongly than bare metals. The binding of Fe to 4N-GQDs is the weakest (5.4 eV), and those of Ca^{2+} and Cr^{2+} are the strongest (20.4 eV). For bare metal-doped 4N-GQDs, the metal binding is unaltered with the field strength, while the binding of metal ions to 4N-GQDs can be strengthened or weakened when applying an electric field, depending on the types of metal ions. The applied electric field also affects the molecular structure of 4N-GQDs and six M–4N-GQDs. These structures are curved when applied and according to the electric field strength, see Fig. 4 and 5. From geometries, the curving is observed from the variation of *Z* coordinates (ΔZ). The curving of the structure is more recognized along the C–C bond direction. The plot of ΔZ with a field strength of 4N-GQDs and M–4N-GQDs shows the quadratic nature. Quadratic equations with relation $y = ax^2 + bx + c$ were obtained for 4N-GQD and six M–4N-GQDs. From the relation, we estimated the largest bending angle (θ) representing the curving of the structure. There is a linear relation between θ and the absolute value of the coefficient *a* or |*a*|. Thus, |*a*| denotes the degree of curvature of the structure. The dependency of field strength on |*a*| is realized. The field strength dependent on |*a*| does not significantly vary with the types of metals/metal ions. The curving of graphene quantum dots when applying an external electric field is facilitated by the large dipole moment of the structure. The deformation energy of six M–4N-GQDs was determined. The deformation energy of M–4N-GQDs varies with field strength (EF) and the type of metal. A value as large as 42 eV was spotted (Fe–4N-GQD at EF = ±0.030 a.u.). The field strength dependence of deformation energy suggested that the instability of M–4N-GQDs was caused by the curvature of the structure. For most M–4N-GQDs, the dipole interaction ($-\mu F$), which stabilizes the molecule under an external electric field (*F*), has a value larger than the deformation energy at the same *F*. This supports the dipole stabilization for curved graphene quantum dots. From our analysis of deformation energy, we also found that Ca^{2+}–4N-GQDs could be curved without applying an external electric field. Furthermore, the HOMO–LUMO gap of metal- and metal ion-doped 4N-GQDs can be altered by an electric field ranging between 1.64 and 2.98 eV, which is lower than those of GQDs and 4N-GQDs. The sudden drop of the HOMO–LUMO gap when the EF was beyond |0.020| a.u. was discovered. We suggest that both the curvature and electronic properties of metal- and metal ion-doped 4N-GQDs could be manipulated by applying an external electric field. This method could hold potential for widespread applications in semiconductor technology.

Author contributions

Thanawit Kuamit: writing, original draft, data curation, visualization, conceptualization, and investigation. Wilasinee Santiwarodom: writing, review & editing, methodology, and visualization. Pavee Apilardmongkol: writing, review & editing, and methodology. Sirilak Kongkaew: writing, review & editing, and investigation. Vudhichai Parasuk: conceptualization, writing, review & editing, and supervision.

Conflicts of interest

The authors declare that they have no known competing financial interests or personal relationships that could have appeared to influence the work reported in this paper.

Data availability

The data supporting this article have been included as part of the SI. See DOI: https://doi.org/10.1039/d5cp02152a

Acknowledgements

This research is supported by the Ratchadapisek Somphot Fund for a Postdoctoral Fellowship, Chulalongkorn University, Thailand, and the Thailand Science Research and Innovation Fund, Chulalongkorn University (BCG_FF_68_376_2300_099), Thailand. We sincerely appreciate the support of the Center of Excellence in Computational Chemistry (CECC), Department of Chemistry, Chulalongkorn University, the National Electronics and Computer Technology Center (NECTEC) under the National e-Science Consortium, and the NSTDA Supercomputer Center (ThaiSC) for providing essential computing resources.

References

1 K. S. Novoselov, A. K. Geim, S. V. Morozov, D. Jiang, Y. Zhang, S. V. Dubonos, I. V. Grigorieva and A. A. Firsov, *Science*, 2004, **306**, 666.
2 Y. Chen, Y. Yang, Y. Xian, P. Singh, J. Feng, S. Cui, A. Carrier, K. Oakes, T. Luan and X. Zhang, *ACS Appl. Mater. Interfaces*, 2020, **12**, 352–360.
3 X. Zhang, L. Luo, L. Li, Y. He, W. Cao, H. Liu, K. Niu and D. Gao, *Nanomed.: Nanotechnol. Biol. Med.*, 2019, **15**, 142–152.
4 S. Li, K. Huang, Q. Fan, S. Yang, T. Shen, T. Mei, J. Wang, X. Wang, G. Chang and J. Li, *Biosens. Bioelectron.*, 2019, **136**, 91–96.
5 Q. Fan, J. Li, Y. Zhu, Z. Yang, T. Shen, Y. Guo, L. Wang, T. Mei, J. Wang and X. Wang, *ACS Appl. Mater. Interfaces*, 2020, **12**, 4797–4803.
6 F. Urban, G. Lupina, A. Grillo, N. Martucciello and A. D. Bartolomeo, *Nano Express*, 2020, **1**, 010001.
7 T. Kuamit, M. Ratanasak, C. Rungnim and V. Parasuk, *J. Mol. Model.*, 2017, 23.
8 T. Chen, C. Liu, P. Mu, H. Sun, Z. Zhu, W. Liang and A. Li, *Chem. Eng. J.*, 2020, **382**, 122831.
9 H.-Y. Wu, S.-T. Li, Y.-W. Shao, X.-Z. Jin, X.-D. Qi, J.-H. Yang, Z.-W. Zhou and Y. Wang, *Chem. Eng. J.*, 2020, **379**, 122373.
10 Y. Zhang, Y. An, L. Wu, H. Chen, Z. Li, H. Dou, V. Murugadoss, J. Fan, X. Zhang, X. Mai and Z. Guo, *J. Mater. Chem. A*, 2019, **7**, 19668–19675.
11 S. K. Krishnan, E. Singh, P. Singh, M. Meyyappan and H. S. Nalwa, *RSC Adv.*, 2019, **9**, 8778–8881.
12 V. Murugadoss, J. Lin, H. Liu, X. Mai, T. Ding, Z. Guo and S. Angaiah, *Nanoscale*, 2019, **11**, 17579–17589.
13 M. M. Tavakoli, R. Tavakoli, P. Yadav and J. Kong, *J. Mater. Chem. A*, 2019, **7**, 679–686.
14 F. Yu, Y. Shi, W. Yao, S. Han and J. Ma, *J. Power Sources*, 2019, **412**, 366–373.
15 H. Hu, X. Yang, X. Guo, K. Khaliji, S. R. Biswas, F. J. García de Abajo, T. Low, Z. Sun and Q. Dai, *Nat. Commun.*, 2019, **10**, 1131.
16 J. Ni, M. Quintana and S. Song, *Phys. E*, 2020, **116**, 113768.
17 G. M. Meconi, R. Tomovska and R. Zangi, *J. CO_2 Util.*, 2019, **32**, 92–105.
18 Z. Bo, X. Guo, X. Wei, H. Yang, J. Yan and K. Cen, *Phys. E*, 2019, **109**, 156–163.
19 S. Kumar and N. Krenner, *J. Sci. Educ. Technol.*, 2002, **11**, 229–236.
20 A. A. F. Husain, W. Z. W. Hasan, S. Shafie, M. N. Hamidon and S. S. Pandey, *Renewable Sustainable Energy Rev.*, 2018, **94**, 779–791.
21 Y. Shimizu and M. Egashira, *MRS Bull.*, 2013, **24**, 18–24.
22 M. A. Rahman, *ASRJETS*, 2014, **7**, 50–70.
23 D. Garrido-Diez and I. Baraia, 2017.
24 S. de-la-Huerta-Sainz, A. Ballesteros and N. A. Cordero, *Journal*, 2023, 13.
25 S.-L. Chang, B.-R. Wu, P.-H. Yang and M.-F. Lin, *Phys. Chem. Chem. Phys.*, 2012, **14**, 16409–16414.
26 N. Pattarapongdilok and V. Parasuk, *Comput. Theor. Chem.*, 2018, **1140**, 86–97.
27 W. Bao, F. Miao, Z. Chen, H. Zhang, W. Jang, C. Dames and C. N. Lau, *Nat. Nanotechnol.*, 2009, **4**, 562–566.
28 T. Georgiou, L. Britnell, P. Blake, R. V. Gorbachev, A. Gholinia, A. K. Geim, C. Casiraghi and K. S. Novoselov, *Appl. Phys. Lett.*, 2011, **99**, 093103.
29 Z. Zhang, B. Liu, K.-C. Hwang and H. Gao, *Appl. Phys. Lett.*, 2011, **98**, 121909.
30 F. Du, J. Huang, H. Duan, C. Xiong and J. Wang, *Sci. Rep.*, 2016, **6**, 25653.
31 F. Banhart, J. X. Li and A. V. Krasheninnikov, *Phys. Rev. B: Condens. Matter Mater. Phys.*, 2005, **71**, 241408.
32 J. Ma, D. Alfè, A. Michaelides and E. Wang, *Phys. Rev. B: Condens. Matter Mater. Phys.*, 2009, **80**, 033407.
33 J. C. Meyer, C. Kisielowski, R. Erni, M. D. Rossell, M. F. Crommie and A. Zettl, *Nano Lett.*, 2008, **8**, 3582–3586.
34 F. Banhart, J. Kotakoski and A. V. Krasheninnikov, *ACS Nano*, 2011, **5**, 26–41.
35 M. Cheng, R. Yang, L. Zhang, Z. Shi, W. Yang, D. Wang, G. Xie, D. Shi and G. Zhang, *Carbon*, 2012, **50**, 2581–2587.
36 L. Ci, L. Song, C. Jin, D. Jariwala, D. Wu, Y. Li, A. Srivastava, Z. F. Wang, K. Storr, L. Balicas, F. Liu and P. M. Ajayan, *Nat. Mater.*, 2010, **9**, 430–435.
37 Y. Wang, Y. Shao, D. W. Matson, J. Li and Y. Lin, *ACS Nano*, 2010, **4**, 1790–1798.
38 D. Cortés-Arriagada, N. Villegas-Escobar and D. E. Ortega, *Appl. Surf. Sci.*, 2018, **427**, 227–236.
39 Q. Wang, Y. Ji, Y. Lei, Y. Wang, Y. Wang, Y. Li and S. Wang, *ACS Energy Lett.*, 2018, **3**, 1183–1191.
40 M. Mahendran, B. Rekha, S. Seenithurai, R. K. Pandyan and S. V. Kumar, *Funct. Mater. Lett.*, 2017, **10**, 1750023.
41 T. Kuamit, F. Mulya, S. Kongkaew and V. Parasuk, *Comput. Theor. Chem.*, 2025, **1244**, 115050.
42 S. Agrawal, A. Srivastava and G. Kaushal, *Solid State Commun.*, 2024, **380**, 115389.
43 I. M. Felix, F. M. Andrade, C. F. Woellner, D. S. Galvão and R. M. Tromer, *Chem. Phys. Lett.*, 2024, **856**, 141604.

44 X. Cao, X.-F. Li and W. Hu, *Chem. – Asian J.*, 2018, **13**, 3239–3245.
45 L. E. Jiménez-Ramírez, D. C. Camacho-Mojica, E. Muñoz-Sandoval and F. López-Urías, *Carbon*, 2017, **116**, 381–390.
46 L. Qu, Y. Liu, J.-B. Baek and L. Dai, *ACS Nano*, 2010, **4**, 1321–1326.
47 Z. Luo, S. Lim, Z. Tian, J. Shang, L. Lai, B. MacDonald, C. Fu, Z. Shen, T. Yu and J. Lin, *J. Mater. Chem.*, 2011, **21**, 8038–8044.
48 C. M. Welch and R. G. Compton, *Anal. Bioanal. Chem.*, 2006, **384**, 601–619.
49 J. Mérian, J. Gravier, F. Navarro and I. Texier, *Molecules*, 2012, **17**, 5564–5591.
50 H. Chen, Z. Wang, S. Zong, P. Chen, D. Zhu, L. Wu and Y. Cui, *Nanoscale*, 2015, **7**, 15477–15486.
51 S. Y. Lim, W. Shen and Z. Gao, *Chem. Soc. Rev.*, 2015, **44**, 362–381.
52 D. Zhang, L. Wen, R. Huang, H. Wang, X. Hu and D. Xing, *Biomater.*, 2018, **153**, 14–26.
53 M. Li, T. Chen, J. J. Gooding and J. Liu, *ACS Sens.*, 2019, **4**, 1732–1748.
54 X. Zhang, C. Wei, Y. Li and D. Yu, *Trends Anal. Chem.*, 2019, **116**, 109–121.
55 H. Shen, *J. Nanomater. Mol. Nanotechnol.*, 2012, 01.
56 Z. Wang, *Carbon*, 2009, **47**, 3050–3053.
57 H. Li, X. Yu, X. Shen, G. Tang and K. Han, *J. Phys. Chem. C*, 2019, **123**, 20020–20025.
58 T. Kuamit and V. Parasuk, *Chem. Phys. Lett.*, 2022, 140050.
59 K. Bhattacharyya, A. Surendran, C. Chowdhury and A. Datta, *Phys. Chem. Chem. Phys.*, 2016, **18**(45), 31160–31167.
60 M. J. Frisch, G. W. Trucks, H. B. Schlegel, G. E. Scuseria, M. A. Robb, J. R. Cheeseman, G. Scalmani, V. Barone, G. A. Petersson, H. Nakatsuji, X. Li, M. Caricato, A. V. Marenich, J. Bloino, B. G. Janesko, R. Gomperts, B. Mennucci, H. P. Hratchian, J. V. Ortiz, A. F. Izmaylov, J. L. Sonnenberg, D. Williams-Young, F. Ding, F. Lipparini, F. Egidi, J. Goings, B. Peng, A. Petrone, T. Henderson, D. Ranasinghe, V. G. Zakrzewski, J. Gao, N. Rega, G. Zheng, W. Liang, M. Hada, M. Ehara, K. Toyota, R. Fukuda, J. Hasegawa, M. Ishida, T. Nakajima, Y. Honda, O. Kitao, H. Nakai, T. Vreven, K. Throssell, J. A. Montgomery Jr., J. E. Peralta, F. Ogliaro, M. J. Bearpark, J. J. Heyd, E. N. Brothers, K. N. Kudin, V. N. Staroverov, T. A. Keith, R. Kobayashi, J. Normand, K. Raghavachari, A. P. Rendell, J. C. Burant, S. S. Iyengar, J. Tomasi, M. Cossi, J. M. Millam, M. Klene, C. Adamo, R. Cammi, J. W. Ochterski, R. L. Martin, K. Morokuma, O. Farkas, J. B. Foresman and D. J. Fox, *Gaussian 16, Revision C.01*, Gaussian, Inc., Wallington CT, 2016.
61 P. A. Denis, *J. Phys. Chem. C*, 2013, **117**, 3895–3902.
62 W. Santiwarodom, P. Apilardmongkol, T. Kuamit and V. Parasuk, *Phys. Chem. Chem. Phys.*, 2024, **26**, 24068–24077.
63 J. D. Thrower, L. Nilsson, B. Jørgensen, S. Baouche, R. Balog, A. C. Luntz, I. Stensgaard, E. Rauls and L. Hornekær, *EAS Publ. Ser.*, 2011, **46**, 453–460.
64 H. Andrews, A. Candian and A. G. G. M. Tielens, *Astron. Astrophys.*, 2016, 595.